Shell-model description for the properties of the forbidden β^- decay in the region "northeast" of ^{208}Pb

Shweta Sharma [1], Praveen C. Srivastava [1,*], Anil Kumar [1] and Toshio Suzuki [2]

[1] *Department of Physics, Indian Institute of Technology Roorkee, Roorkee 247667, India*

[2] *Department of Physics, College of Humanities and Sciences, Nihon University, Sakurajosui 3, Setagaya-ku, Tokyo 156-8550, Japan*

(Received 23 June 2022; accepted 12 August 2022; published 29 August 2022)

We report a comprehensive shell-model study of the log ft values for the forbidden β^- decay transitions in the region northeast of ^{208}Pb. For this we have considered $^{210-215}$Pb $\rightarrow$ $^{210-215}$Bi and $^{210-215}$Bi $\rightarrow$ $^{210-215}$Po transitions. We have performed shell-model calculation using the KHPE interaction in valence shells 82-126 for protons and 126-184 for neutrons without any truncation. We have also calculated half-lives and Q values for the concerned nuclei. Recently several log ft values were observed corresponding to β^- decay from the (8^-) isomeric state of ^{214}Bi^m at the CERN-ISOLDE facility [Andel *et al.*, Phys. Rev. C **104**, 054301 (2021)], and for the first time we have reported shell-model results for these transitions.

DOI: 10.1103/PhysRevC.106.024333

I. INTRODUCTION

The r process plays a significant role in the nucleosynthesis of heavier nuclei in astrophysics [1]. It is believed to occur in core-collapse supernovae [2] or neutron star mergers [3], but the actual site of r-process nucleosynthesis is still an open area for investigation [4]. The main conditions required for the r-process nucleosynthesis [5] are high temperature and large neutron density [6,7]. Further, the abundance pattern of r-process nuclei shows enhanced peaks near neutron shell closures. ^{208}Pb is the heaviest doubly magic stable nucleus with 82 protons and 126 neutrons. Due to the increased stability of doubly magic nuclei compared to the single magic nuclei and others, the region around these nuclei has always been an area of great interest for investigation. The measurement of half-lives of nuclei near $N = 126$ is difficult. Thus, it is highly desirable to give theoretical predictions for half-lives around this region. Suzuki *et al.* [8] have evaluated beta-decay properties of r-process nuclei near $N = 126$ isotones using shell-model calculations. First forbidden beta decay competes with allowed Gamow-Teller (GT) and Fermi beta decay in the region of $N = 126$ r-process nuclei [9,10]. It is thus crucial to study these nuclei in this region for a better understanding of the abundance pattern of these r-process nuclei.

Beta-decay can be divided into two categories: allowed and forbidden, based on the value of the angular momentum of the emitted leptons. Allowed transitions correspond to no change in parity and the $l = 0$ state of the emitted leptons relative to the nucleus, while $l > 0$ corresponds to the forbidden transitions. Further, based on the value of spin angular momentum, these transitions can be characterized in two categories, Fermi and GT transitions. Fermi transitions correspond to spin nonflip with $S = 0$, whereas GT transitions correspond to spin flip with $S = 1$. Further, forbidden transitions can be divided into unique forbidden beta decay and nonunique forbidden beta decay. In unique forbidden beta decay $\Delta J = l + 1$, while in nonunique forbidden beta decay $\Delta J = l - 1, l$, where l is the degree of forbiddenness. Change in parity for forbidden beta decay is positive (even) for an even degree of forbiddenness, while it is negative (odd) for an odd degree of forbiddenness. Beta-decay properties have been evaluated using effective values of the weak coupling constants in Refs. [11,12]. Recently, using the shell model, our group calculated first-forbidden beta-decay properties of ^{207}Hg $\rightarrow$ ^{207}Tl in Ref. [13].

There are several approaches that can be used to calculate beta-decay properties. One is the macroscopic approach, i.e., the gross theory of beta decay [14], and the other is the microscopic approach, such as the quasiparticle random phase approximation (QRPA) [15], density functional theory (DFT) [16], Hartree-Fock-Bogoliubov method (HFB) [17], etc. These models underestimate the residual interaction between nucleons, which reduces the Gamow-Teller (GT) strengths towards lower excitation energies [18–20]. There is another approach, i.e., the shell model. We are using a large-scale shell model in the study of beta-decay properties. Further, in the shell model, quenching factors for the weak axial and vector coupling constants are needed to reproduce reliable data [21,22]. Several efforts have been made to calculate quenching factors in the Pb region: Warburton [23] found that the quenching factors for the axial and vector coupling constants are different, and come out to be $(g_A/g_A^{\text{free}}, g_V/g_V^{\text{free}}) = (0.47, 0.64)$ in the Pb region. Further, the mesonic enhancement factor was calculated in Refs. [24,25] for the first forbidden beta decay with $\Delta J^\pi = 0^-$ for $A = 205$–212, where the enhancement factor is defined as the proportion of the axial-charge matrix element γ_5 in first-forbidden beta decay to its impulse-approximation value. This value comes out to be $\epsilon_{\text{MEC}} = 1 + \delta_{\text{MEC}} = 2.01 \pm 0.05$. Later, Rydstrom *et al.* in Ref. [26] found two sets of quenching factors in the

*Corresponding author: praveen.srivastava@ph.iitr.ac.in

Pb region: one is $(g_A/g_A^{free}, g_V/g_V^{free}) = (0.34, 0.67)$ and the other is $(g_A/g_A^{free}, g_V/g_V^{free}) = (0.51, 0.30)$. Furthermore, Zhi *et al.* [27] performed large-scale shell-model calculations for *r*-process waiting point nuclei with $N = 50, 82, 126$, including both GT and first forbidden transitions. They found that the shell model overestimate the transition strengths in the GT and forbidden beta decays. Thus, they found the quenching factors $(g_A/g_A^{free}, g_V/g_V^{free}) = (0.38, 0.51)$.

In the present work, the log ft values, average shape factor, and half-lives were calculated for $^{210-215}$Pb $\rightarrow$ $^{210-215}$Bi and $^{210-215}$Bi $\rightarrow$ $^{210-215}$Po transitions and compared with the available experimental data. These beta-decay properties were computed using two sets of quenching factors: one calculated from our work using the chi-squared fitting method, and the other taken from Ref. [27]. To the best of our knowledge, theoretical estimates for these nuclei mentioned were carried out for the first time except for log ft values for ^{211}Pb to ^{211}Bi transitions [24], which were calculated by using old experimental data with a truncated model space using the KHPE interaction [28]. In our work, we have performed large-scale shell-model calculations without using any truncation. Since β decay is very sensitive to the Q value, it is crucial to use a precise Q value. Thus, we have also calculated Q values using shell-model calculations and used them in the calculation of beta-decay properties. The shell-model results were also calculated where experimental data are not available. Based on our calculated log ft values, we have confirmed spin and parity of several states where experiments were unable to make unique assignments.

Recently, a new experiment was performed at the CERN-ISOLDE facility to study the ^{214}Bi isotope using γ ray spectroscopy, and a new isomeric state (8^-) was identified. Further, beta decay of this ^{214}Bi^m isomer to various spin-parity states of ^{214}Po was studied, and its log ft values and beta-decay feeding fractions were reported. Moreover, the experimental energy spectra of ^{214}Po and yrast and yrare states of ^{214}Bi were compared with the KHPE and H208 interactions, but log ft values using these shell-model interactions were not calculated. Thus, for the first time, these log ft and average shape factor values have been calculated within the framework of shell-model and compared with the experimental values according to the decay mode as presented in Ref. [29].

The content of this paper is organized as follows: Section II depicts the theoretical formalism in which the shell-model Hamiltonian, beta-decay theory, and quenching factor are briefly discussed. Further, the calculation of the quenching factor with the help of the chi-squared fitting method is given in this section. In Sec. III, log ft values, average shape factors, and half-lives for the concerned nuclei are evaluated, and computations of Q values are also carried out. Finally, the conclusion is given in Sec. IV.

II. FORMALISM

A. Shell-model Hamiltonian

The nuclear shell-model Hamiltonian can be expressed as combination of a single-particle energy term and a two-nucleon interaction term [30]. The shell-model Hamiltonian has the form

$$H = T + V = \sum_{\alpha} \epsilon_\alpha c_\alpha^\dagger c_\alpha + \frac{1}{4} \sum_{\alpha\beta\gamma\delta} v_{\alpha\beta\gamma\delta} c_\alpha^\dagger c_\beta^\dagger c_\delta c_\gamma, \quad (1)$$

where $\alpha = \{n, l, j, t\}$ stands for single-particle state and the corresponding single-particle energy is denoted by ϵ_α. $c_\alpha^\dagger$ and c_α stand for creation and annihilation operators. $v_{\alpha\beta\gamma\delta} = \langle \alpha\beta | V | \gamma\delta \rangle$ are the antisymmetrized two-body matrix elements.

B. β-decay theory for allowed and forbidden transitions

The theoretical formalism of beta-decay theory is briefly explained here. Here, we will give brief details of the formalism about allowed and forbidden beta decay. One can find more detailed formalisms in Refs. [31,32]. This formalism is based on the impulse approximation [30], i.e., the decaying nucleon does not feel strong interaction with the remaining nucleons and only feels weak interaction at the instance of decay. Here, the remaining nucleons will act as spectator. The total half-life is the inverse of the decay rate, and it can be defined as

$$\frac{1}{T_{1/2}} = \sum_k \frac{1}{t_{1/2}^{(k)}}, \quad (2)$$

where $t_{1/2}^{(k)}$ is the partial half-life to the final state k. The partial half-life is related to transition probability as

$$t_{1/2} = \frac{\ln(2)}{\int_{m_e c^2}^{W_0} P(W_e) dW_e}, \quad (3)$$

where the integrand in the denominator is the transition probability, and m_e is the electron mass. The probability of the emitted beta particle to have energy between W_e and $W_e + dW_e$ has the form

$$P(W_e)dW_e = \frac{G_F^2}{(\hbar c)^6} \frac{1}{2\pi^3 \hbar} C(W_e) p_e c W_e (W_0 - W_e)^2 \times F_0(Z, W_e) dW_e, \quad (4)$$

where G_F is the effective coupling constant, i.e., the Fermi coupling constant determining the strength of the beta interaction, and p_e and W_e are the momentum and energy of the emitted beta particle, respectively. W_0 is the endpoint energy, i.e., the maximum energy attained by the emitted beta particle in the beta-decay process. The $C(W_e)$ is the shape factor that depends on electron energy, and $F_0(Z, W_e)$ is the Fermi function included in the expression for Coulomb interaction between the beta particle and the remaining nucleus. For the simplification of the integration, dimensionless quantities are introduced such as $w_0 = W_0/m_e c^2$, $w_e = W_e/m_e c^2$, and $p = p_e c/m_e c^2 = \sqrt{(w_e^2 - 1)}$. Thus, the dimensionless integrated shape function has the form

$$f = \int_1^{w_0} C(w_e) p w_e (w_0 - w_e)^2 F_0(Z, w_e) dw_e. \quad (5)$$

The shape factor does not depends on electron energy in case of allowed transition, i.e., $C(w_e) = B(\mathrm{GT})$, where $B(\mathrm{GT})$

is the Gamow-Teller reduced transition probability. Thus,

$$C(w_e) = \frac{g_A^2}{2J_i+1}|\mathcal{M}_{\rm GT}|^2, \tag{6}$$

where the J_i is the initial angular momentum and g_A is the axial-vector coupling constant, and $\mathcal{M}_{\rm GT}$ stands for the Gamow-Teller nuclear matrix element [33].

Thus, the phase-space factor becomes

$$f_0 = \int_1^{w_0} p w_e (w_0 - w_e)^2 F_0(Z, w_e) dw_e. \tag{7}$$

For forbidden beta decay, the shape factor is given by

$$C(w_e) = \sum_{k_e,k_\nu,K} \lambda_{k_e}\Big[M_K(k_e,k_\nu)^2 + m_K(k_e,k_\nu)^2 - \frac{2\gamma_{k_e}}{k_e w_e} M_K(k_e,k_\nu) m_K(k_e,k_\nu)\Big], \tag{8}$$

where K is the forbiddenness order as well as the angular momentum transfer and k_e and k_ν are the positive integers emerging from partial wave expansion of the leptonic wave function. The quantities $M_K(k_e,k_\nu)$ and $m_K(k_e,k_\nu)$ are complicated combinations of the different form factors $F_{KLS}(q^2)$ containing nuclear structure information and the leptonic phase space factors. They are expansions in a set of small quantities $\{\alpha Z, p_eR/\hbar, p_\nu R/\hbar, m_e cR/\hbar, W_eR/\hbar c\}$. Two distinct sums that satisfy $k_e + k_\nu = K+1$ and $k_e + k_\nu = K+2$ are taken in Eq. (8). Equation (8) is the case in which the angular momentum transfer ΔJ is equal to K, for example, for the first-forbidden transition with $\Delta J^\pi = 1^-$ and $K = 1$. When $\Delta J = K+1$, the additional terms $M_{K+1}(k_e,k_\nu)$ with $k_e + k_\nu = K+2$ need to be included [34]. These terms correspond to the first-forbidden transition with $\Delta J^\pi = 2^-$ with $K = 1$, for example. When $\Delta J = 0$ in the first-forbidden transition, the shape factor is given by $M_0(1,1)^2 + m_0(1,1)^2 - \frac{2\gamma_{k_e}}{k_e w_e} M_0(1,1) \times m_0(1,1)$, where $M_0(1,1)$ and $m_0(1,1)$ are given in Ref. [35] (see Appendix 3 also). More detail about these quantities can be found in Refs. [34,36]. The auxiliary quantities γ_{k_e} and λ_{k_e} can be written as

$$\gamma_{k_e} = \sqrt{k_e^2 - (\alpha Z)^2} \quad \text{and} \quad \lambda_{k_e} = F_{k_e-1}(Z, w_e)/F_0(Z, w_e),$$

where λ_{k_e} stands for Coulomb function and $F_{k_e-1}(Z, w_e)$ is the generalized Fermi function [34], which has the form

$$F_{k_e-1}(Z, w_e) = 4^{k_e-1}(2k_e)(k_e+\gamma_{k_e})[(2k_e-1)!!]^2 e^{\pi y} \times \left(\frac{2p_eR}{\hbar}\right)^{2(\gamma_{k_e}-k_e)} \left(\frac{|\Gamma(\gamma_{k_e}+iy)|}{\Gamma(1+2\gamma_{k_e})}\right)^2. \tag{9}$$

The auxiliary quantity $y = (\alpha Z w_e/p_e c)$, where $\alpha = 1/137$ is the fine structure constant.

The form factor can be expanded in the form of power series of the quantity $qR/\hbar$, where $q = |p_e + p_\nu|$ denotes the momentum transfer and R denotes the nuclear radius. Thus, form factor can be written as

$$F_{KLS}(q^2) = \sum_N \frac{(-1)^N(2L+1)!!}{(2N)!!(2L+2N+1)!!}(qR/\hbar)^{2N} F_{KLS}^{(N)} = F_{KLS}^{(0)} - \frac{(qR)^2}{2(2L+3)} F_{KLS}^{(1)}. \tag{10}$$

The higher order terms, i.e., $N = 2, 3, 4, \ldots$ can be ignored because contributions of the momenta of the participating leptons is small. The $F_{KLS}^{(N)}$ are the form factor coefficients, with L, S, and K the ranks of orbital, spin, and total transition operators, respectively. Using the impulse approximation, the nuclear form factor coefficients can be replaced by nuclear matrix elements (NMEs) in the form

$$R^{LV} F_{KLS}^{(N)}(k_e,m,n,\rho) = (-1)^{K-L} g_V\, {}^V\mathcal{M}_{KLS}^{(N)}(k_e,m,n,\rho), \tag{11}$$

$$R^{LA} F_{KLS}^{(N)}(k_e,m,n,\rho) = (-1)^{K-L+1} g_A\, {}^A\mathcal{M}_{KLS}^{(N)}(k_e,m,n,\rho). \tag{12}$$

Here, m is the total power of $(m_eR/\hbar)$, $(W_eR/\hbar)$, and αZ, n is the total power of $(W_eR/\hbar)$ and αZ, and ρ is the power of αZ [34]. (The shape form factors for the forbidden transition are given in the Appendix using the NMEs.) ${}^{V/A}\mathcal{M}_{KLS}^{(N)}(k_e,m,n,\rho)$ are the NMEs [37,38], which can be described as

$$ {}^{V/A}\mathcal{M}_{KLS}^{(N)}(pn)(k_e,m,n,\rho) = \frac{\sqrt{4\pi}}{\widehat{J_i}} \sum_{pn} {}^{V/A}m_{KLS}^{(N)}(pn)(k_e,m,n,\rho) \times (\Psi_f \parallel [c_p^\dagger \tilde{c}_n]_K \parallel \Psi_i), \tag{13}$$

where $\widehat{J_i} = \sqrt{2J_i+1}$ with J_i being the initial angular momentum, and the summation runs over proton and neutron single-particle states. The quantity ${}^{V/A}m_{KLS}^{(N)}(pn)(k_e,m,n,\rho)$ stands for the single-particle matrix elements (SPMEs), and is independent of the choice of nuclear models. $(\Psi_f||[c_p^\dagger\tilde{c}_n]_K||\Psi_i)$ is the one-body transition density (OBTD), which varies for different nuclear models. Here, (Ψ_i) and (Ψ_f) are the initial and final nuclear states. The SPMEs are calculated with the help of the formalism given in Ref. [35], whereas the OBTDs are calculated from the shell-model using NUSHELLX [39] and KSHELL [40]. The product of partial half-life and the dimensionless integrated shape function is given by,

$$ft_{1/2} = \kappa, \tag{14}$$

where κ is constant value which is expressed as [41]

$$\kappa = \frac{2\pi^3\hbar^7 \ln(2)}{m_e^5 c^4 (G_{\rm F}\cos\theta_{\rm C})^2} = 6289\ \text{s}, \tag{15}$$

where $\theta_{\rm C}$ is the Cabibbo angle which is the mixing angle between two generation of quarks.

Usually, ft values are expressed in terms of $\log ft$ values because ft values are large. Thus,

$$\log ft \equiv \log(f_0 t_{1/2}).$$

The phase space factor is sensitive to the Q value. Therefore, it is essential to evaluate it precisely. Thus, the Q value [42] can be expressed as

$$Q(\beta^-) = E^{\rm par}_{g.s.} - E^{\rm dau}_{g.s.} + \delta m, \tag{16}$$

where $\delta m = (m_n - m_p - m_e)c^2 = 0.78$ MeV. $E^{\rm par}_{g.s.}$ and $E^{\rm dau}_{g.s.}$ stand for ground state binding energies of the parent and daughter nuclei, respectively. The binding energy of the ground state is given by

$$E = E_{\rm SM} + E_{\rm core} + E_C(Z, N). \tag{17}$$

Here $E_{\rm SM}$ is the shell-model calculated binding energy and $E_{\rm core}$ is the binding energy of the core considered, and $E_C(Z, N)$ is the Coulomb energy which can be calculated from the formalism given in Refs. [43,44].

C. Quenching factor

In beta decay, the Gamow-Teller and forbidden strengths get overestimated in the shell-model calculations. The weak coupling constants $g_{\rm V}$ and $g_{\rm A}$ are included in these Gamow-Teller and forbidden strengths, where $g_{\rm V}$ is the vector coupling constant determined by CVC (conserved vector current) theory and $g_{\rm A}$ is the axial-vector coupling constant determined by PCAC (partial axial-vector current) theory. The free nucleon values of these weak coupling constants are $g_{\rm V} = 1.0$ and $g_{\rm A} = 1.27$. These values get affected by many nucleon correlations like model space truncation in shell-model calculations and other nuclear medium effects. Therefore, the values of weak coupling constants get heavily quenched in the heavier mass region. Thus, we use effective values of these weak coupling constants. According to Behrens and Bühring [31], the average shape factor is given by

$$\overline{C(w_e)} = f/f_0. \tag{18}$$

Here f is the phase space factor and f_0 is the phase space factor for allowed transitions. For allowed GT transitions, this shape factor is independent of electron energy. However, for nth forbidden transition, the average shape factor [24] comes out to be

$$\overline{C(w_e)}({\rm fm}^{2n}) = \frac{6289\lambda\!\!\!^{-2n}_{\rm Ce}}{ft}. \tag{19}$$

Thus, for the first forbidden transition, the average shape factor [45] has the form

$$\overline{C(w_e)}({\rm fm}^2) = \frac{6289\lambda\!\!\!^{-2}_{\rm Ce}}{ft} = \frac{9378 \times 10^5}{ft}, \tag{20}$$

where $\lambda\!\!\!^{-}_{\rm Ce}$ is the reduced Compton wavelength of electron. Now, for allowed GT transitions, the operator is just $\boldsymbol{\sigma\tau}$, whereas there are six nuclear matrix elements (NMEs) for the first forbidden transition [30]. Out of these, four nonrelativistic NMEs are extracted from wave-function expansion of p-wave leptons, and rest two relativistic NMEs come from the small components of Dirac spinors. These are

$$\begin{aligned} &O(0^-) : O_{\rm RA} = g_{\rm A}(\boldsymbol{\sigma}\cdot\boldsymbol{p_e}), \quad O_{\rm SA} = {\rm g_A}(\boldsymbol{\sigma}\cdot\boldsymbol{r}),\\ &O(1^-) : O_{\rm RV} = g_{\rm V}\boldsymbol{p_e}, \quad O_{\rm VA} = {\rm g_A}(\boldsymbol{\sigma}\times\boldsymbol{r}), \quad O_{\rm VV} = {\rm g_V}\boldsymbol{r},\\ &O(2x^-) : O_{\rm TA} = g_{\rm A}[\boldsymbol{\sigma r}]_2, \end{aligned} \tag{21}$$

where $O(0^-)$ is rank zero operator with ΔJ=0. The terms $O_{\rm RA}$ and $O_{\rm SA}$ are the recoil-axial matrix element and scalar-axial matrix element, respectively. $O(1^-)$ is rank-1 operator with $\Delta J = 1$. The terms $O_{\rm RV}$, $O_{\rm VA}$, and $O_{\rm VV}$ are the recoil-vector matrix element, vector-axial matrix element, and vector-vector matrix element, respectively. $O(2^-)$ is rank-2 operator with $\Delta J = 2$. The term $O_{\rm TA}$ is the tensor-axial matrix element. These six operators change parity during transition, i.e., $\pi_i\pi_f = -1$. Further, the recoil-axial matrix element γ_5 gets enhanced over the impulse approximation with the aid of a mesonic enhancement factor [46], which is denoted by $\epsilon_{\rm MEC}$. We have used the value $\epsilon_{\rm MEC} = 2.01$ of mesonic enhancement factor in these calculations for the rank-0 nuclear matrix element γ_5 which corresponds to $\epsilon_{\rm MEC} = 2.01 \pm 0.05$ given in [24].

We obtained the quenching factor for $^{210\text{–}215}$Pb $\rightarrow$ $^{210\text{–}215}$Bi and $^{210\text{–}215}$Bi $\rightarrow$ $^{210\text{–}215}$Po transitions using the chi-square fitting method. We compared theoretical and experimental average shape factor values for these transitions to get the quenching factor. In our calculation for the average shape factor, we included the next-to-leading order terms [47]. First we performed calculations without including the quenching factor by taking the bare values of the weak coupling constant, i.e., $g_A = 1.27$ and $g_V = 1.00$. Corresponding results are shown in Fig. 1(a); we can conclude that the theoretical and experimental values of the average shape factor are very far from each other. Hence, using the chi-square fitting method to obtain the quenching factor, it comes out to be 0.38, such that $g_A^{\rm eff} = q g_A^{\rm free} = 0.4826$ and $g_V^{\rm eff} = 1.00$. Using these values of weak coupling constants, we have plotted Fig. 1(b) for the same transitions. In this figure, the data points come close to the central line, which means that theoretical values are approaching to the experimental ones. We also calculated values of the average shape factor using another set of weak coupling constants taken from Ref. [27]. Corresponding results are shown in Fig. 1(c) for $(g_{\rm A}/g_{\rm A}^{\rm free}, g_{\rm V}/g_{\rm V}^{\rm free}) = (0.38, 0.51)$. This figure shows the best fit for the average shape factor. In our further calculations, we used these two sets of weak coupling constants, i.e., in set I $(g_{\rm A}/g_{\rm A}^{\rm free}, g_{\rm V}/g_{\rm V}^{\rm free}) = (0.38, 1.00)$, and in set II $(g_{\rm A}/g_{\rm A}^{\rm free}, g_{\rm V}/g_{\rm V}^{\rm free}) = (0.38, 0.51)$.

III. RESULTS AND DISCUSSION

In the present work, large-scale shell-model calculations for the allowed and forbidden beta-decay transitions were carried out in the region northeast of the doubly magic nucleus ^{208}Pb and compared these results with the recently available experimental data [48]. In this work, for the first time, we present theoretical log ft values, average shape factors, and half-lives for $^{210\text{–}215}$Pb $\rightarrow$ $^{210\text{–}215}$Bi and $^{210\text{–}215}$Bi $\rightarrow$ $^{210\text{–}215}$Po transitions. We have also calculated the quenching factors (as discussed in the preceding section) and theoretical Q values for these nuclei, and we have compared the

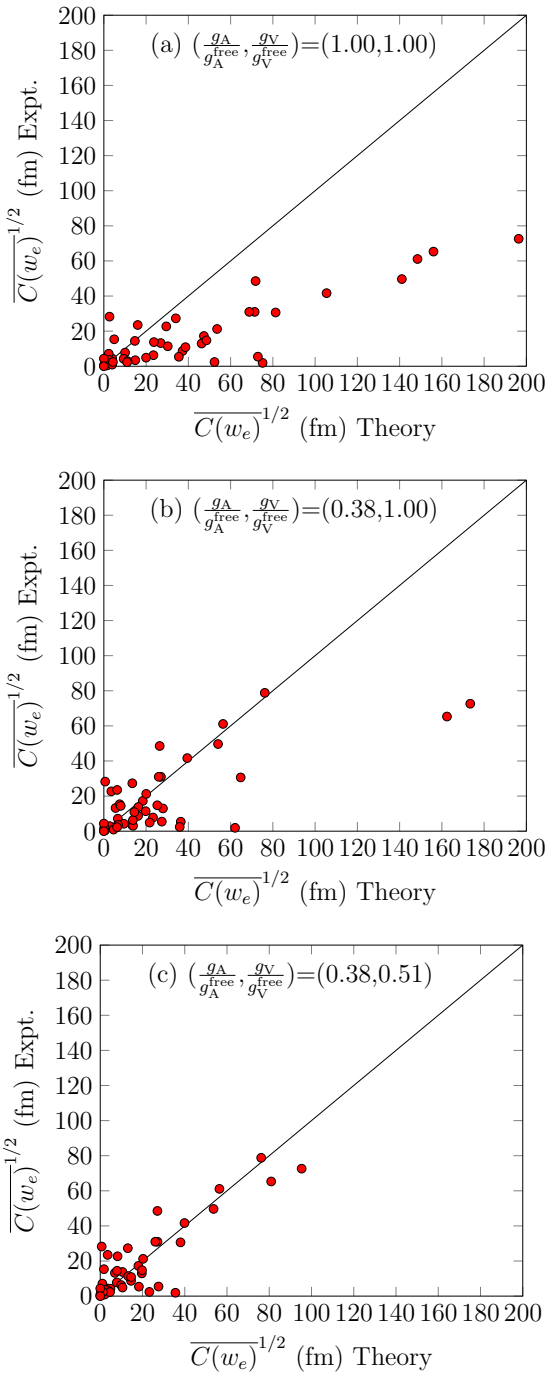

FIG. 1. Comparison of calculated and experimental average shape factors for allowed and first-forbidden transitions by using different values of quenching factors for axial and vector coupling constants.

shell-model results with the experimental data. In the present work we performed shell-model calculations by taking ^{208}Pb as a core using the KHPE effective interaction [28] given by Kuo and Herling for ^{208}Pb ($Z = 82$, $N = 126$). The model space for this interaction is $0h_{9/2}, 1f_{7/2}, 1f_{5/2}, 2p_{3/2}, 2p_{1/2}, 0i_{13/2}$ for protons ($82 < Z < 126$) and $0i_{11/2}, 1g_{9/2}, 1g_{7/2}, 2d_{5/2}, 2d_{3/2}, 3s_{1/2}, 0j_{15/2}$ for neutrons ($126 < N < 184$).

In Table I, log ft values and average shape factors were calculated from the ground states of $^{210-215}$Pb to the ground, and several excited states of $^{210-215}$Bi using both sets of the weak coupling constants. In some places, double parentheses represents those states which are not confirmed experimentally. These results have been computed using experimental Q values taken from [48]. On comparing experimental and theoretical results in Table I, we notice that both sets of weak coupling constants give promising results for the log ft values. We can observe that the log ft value for the transition from ^{210}Pb(0^+) to ^{210}Bi(0_1^-) at energy 46.539(1) keV is 5.469 for both sets, which agrees quite well the experimental value, i.e., 5.4(1). In the case of ^{211}Pb($9/2^+$) to ^{211}Bi($9/2_2^-$) transition at energy 831.960(12) keV, the theoretical value of log ft is 5.779 for set I and 5.771 for set II, which are near the experimental value, i.e., 5.7330(18). Shell-model results for ^{211}Pb to ^{211}Bi transitions have also been calculated by Warburton [24] with the KHPE interaction using old data. Further, for the transition from ^{213}Pb (($9/2^+$)) to ^{213}Bi($9/2_1^-$) the theoretical log ft value for set I is 6.447 and for the set II it is 6.459, while the experimental value is 6.5. In the case of the ^{215}Pb (($9/2^+$)) to ^{215}Bi (($9/2_1^-$)) transition, experimentally, the log ft value should be greater than or equal to 6.1, which is confirmed by shell-model results as the log ft value for set I is 6.713 and for set II it is 6.741. Also, in the ^{215}Pb (($9/2^+$)) to ^{215}Bi (($7/2_1^-$)) transition at energy 183.5(3) keV, this log ft value should be greater than 6.6, which can be verified via theoretical results; i.e., for set I it is 7.224 and for set II it is 8.486. There are several such transitions for which theoretical log ft values match very well with the experimental values, which shows the authenticity of shell-model calculations. We have also calculated log ft results corresponding to the transitions for which experimental data are unavailable. For instance, the log ft value for the ^{212}Pb(0^+) to ^{212}Bi($2_1^{(-)}$) transition at energy 115.183(5) keV is 10.143 for set I and 10.140 for set II. In the case of the ^{214}Pb(0^+) to ^{214}Bi(2_1^-) transition at energy 53.2260(15) keV, this value comes out to be 9.446 for set I and 9.445 for set II, while for the ^{214}Pb(0^+) to ^{214}Bi ((2_4^-)) transition at energy 377.03(4) keV this value comes out to be 10.211 for set I and 10.197 for set II. Furthermore, in case of ^{213}Pb (($9/2^+$)) $\rightarrow$ ^{213}Bi (($7/2_2^-$), ($5/2_1^-$)) at energy 592.72(8) keV, experiments do not confirm one suitable spin state and thus predict two possible spin states. Therefore, we performed shell-model calculations for both possible spin states $7/2_2^-$ and $5/2_1^-$. It is inferred from these results that the spin and parity of the state at 592.72(8) keV is $7/2_2^-$ as its log ft value is 8.184 for set I and 8.018 for set II, which are close to the experimental value, i.e., 7.5. However, for the ^{214}Pb(0^+) to ^{214}Bi(0_1^-, 1_3^-) transition at energy 351.9323(21) keV, our calculated shell-model results for the log ft values give good results for both possible spins of the state. Thus it is difficult to distinguish the spin-parity of these two states. There are some transitions in this table for which shell-model results overestimate or underestimate the experimental log ft values. For instance, for the ^{210}Pb(0^+) to ^{210}Bi(1_1^-) transition the experimental log ft value is 7.9(1), while for set I it is 6.719 and for set II it is 8.517. Similarly, for ^{212}Pb(0^+) to ^{212}Bi($1_1^{(-)}$),

TABLE I. Comparison between theoretical and experimental [48] log ft values for Pb → Bi transitions. The calculations are carried out through two sets of quenching factors in the weak coupling constants g_V and g_A, for set I $(g_A/g_A^{free}, g_V/g_V^{free}) = (0.38, 1.00)$, and for set II $(g_A/g_A^{free}, g_V/g_V^{free}) = (0.38, 0.51)$. The quenching factors of set I were calculated from this work and those in set II were taken from [27]. Here, FNU and FU denotes forbidden nonunique and forbidden unique beta decay, respectively.

Transition				log ft			$[\overline{C(w_e)}]^{1/2}$		
Initial (J_i^π)	Final (J_f^π)	Decay mode	Energy (keV)	Expt.	Set I	Set II	Expt.	Set I	Set II
^{210}Pb(0^+)	^{210}Bi(1_1^-)	1st FNU	0.0	7.9(1)	6.719	8.517	3.436	13.380	1.689
	^{210}Bi(0_1^-)	1st FNU	46.539(1)	5.4(1)	5.469	5.469	61.102	56.422	56.422
^{211}Pb($9/2^+$)	^{211}Bi($9/2_1^-$)	1st FNU	0.0	5.990(8)	6.109	6.106	30.978	27.024	27.104
	^{211}Bi($7/2_1^-$)	1st FNU	404.866(9)	7.19(3)	6.239	7.183	7.781	23.262	7.847
	^{211}Bi($9/2_2^-$)	1st FNU	831.960(12)	5.7330(18)	5.779	5.771	41.644	39.480	39.881
	^{211}Bi($9/2_3^-$)	1st FNU	1109.485(23)	5.58(4)	5.507	5.513	49.665	54.049	53.646
^{212}Pb(0^+)	^{212}Bi($1_1^{(-)}$)	1st FNU	0.0	6.73(4)	7.486	7.288	13.215	5.534	6.952
	^{212}Bi($2_1^{(-)}$)	1st FU	115.183(5)		10.143	10.140		0.260	0.261
	^{212}Bi($0_1^{(-)}$)	1st FNU	238.632(2)	5.179(10)	5.208	5.208	78.805	76.179	76.179
	^{212}Bi($1_2^{(-)}$)	1st FNU	415.272(11)	5.342(17)	4.551	5.156	65.321	162.418	80.915
^{213}Pb ($(9/2^+)$)	^{213}Bi($9/2_1^-$)	1st FNU	0.0	6.5	6.447	6.459	17.221	18.297	18.057
	^{213}Bi ($(7/2_1^-)$)	1st FNU	257.63(7)	7.7	6.719	7.887	4.326	13.386	3.489
	^{213}Bi ($(5/2_1^-)$)	1st FU	592.72(8)	7.5	13.355	13.698	5.446	0.006	0.004
	^{213}Bi ($(7/2_2^-)$)	1st FNU	592.72(8)	7.5	8.184	8.018	5.446	2.477	2.998
	^{213}Bi ($(9/2_2^-)$)	1st FNU	977.71(8)	5.6	6.128	6.107	48.535	26.423	27.065
^{214}Pb(0^+)	^{214}Bi(1_1^-)	1st FNU	0.0	6.26(4)	7.873	7.144	22.701	3.545	8.205
	^{214}Bi(2_1^-)	1st FU	53.2260(15)		9.446	9.445		0.580	0.580
	^{214}Bi ((2_2^-))	1st FU	62.68(5)		8.087	8.098		2.772	2.756
	^{214}Bi ((3_1^-))	3rd FNU	62.68(5)		15.860	14.949		53.652	153.140
	^{214}Bi ((2_3^-))	1st FU	258.869(24)	8.04(12)	8.665	8.688	2.924	1.424	1.387
	^{214}Bi(1_2^-)	1st FNU	295.2236(19)	5.250(24)	4.494	5.014	72.620	173.437	95.335
	^{214}Bi ((0_1^-))	1st FNU	351.9323(21)	5.07(3)	5.080	5.080	89.342	88.348	88.348
	^{214}Bi ((1_3^-))	1st FNU	351.9323(21)	5.07(3)	5.074	6.187	89.342	88.880	24.689
	^{214}Bi ((2_4^-))	1st FU	377.03(4)		10.211	10.197		0.240	0.244
	^{214}Bi ((1_4^-))	1st FNU	533.672(14)	6.23(4)	7.374	7.881	23.499	6.304	3.511
	^{214}Bi(1_1^+)	Allowed	838.994(22)	4.43(9)	4.251	4.251	0.483	0.594	0.594
^{215}Pb ($(9/2^+)$)	^{215}Bi ($(9/2_1^-)$)	1st FNU	0.0	$\geqslant$6.1	6.713	6.741	$\leqslant$27.293	13.472	13.045
	^{215}Bi ($(7/2_1^-)$)	1st FNU	183.5(3)	>6.6	7.224	8.486	<15.348	7.480	1.751

the experimental value is 6.73(4), while it is 7.486 for set I and it is 7.288 for set II. There is one allowed transition from ^{214}Pb(0^+) to ^{214}Bi(1_1^+) at energy 838.994(22) keV. The shell-model log ft value using bare values of weak coupling constants is 3.405, but when we are using effective values of weak coupling constants it comes out to be 4.251 for both of the sets, which is close to the experimental log ft value, i.e., 4.43(9). Its branching fraction is 5.697% in the case of set II using the experimental Q value. Experimentally this value of branching fraction is 2.75(8)%.

Table II shows the log ft and average shape factor values for the transitions from the ground states of $^{210–215}$Bi to the ground and different excited states of $^{210–215}$Po, calculated using both sets of the weak coupling constants. Decay mode and experimental data are also included in this table. The theoretical results are in quite good agreement with the experimental data. For instance, the log ft value for the ^{210}Bi(1^-) to ^{210}Po(0_1^+) transition is 8.114 for set II, which is close to the experimental value, i.e., 8.0. In the case of the ^{211}Bi($9/2^-$) to ^{211}Po($9/2_1^+$) transition, the experimental log ft value is 5.99(2), which is close to the shell-model results; i.e., for set I it is 6.143 and for set II it is 6.140. Also, for the ^{212}Bi($1^{(-)}$) to ^{212}Po(2_4^+) transition at energy 1805.96(10) keV, the theoretical log ft value for set I is 6.546 and for set II it is 6.926, which match with the experimental value, i.e., 6.695(21). For the ^{213}Bi($9/2^-$) to ^{213}Po($9/2_1^+$) transition, this value is 6.367 for set I and 6.358 for set II, which are very near the experimental value, i.e., 6.31(1). On moving toward the transition from ^{214}Bi(1^-) to ^{214}Po(0_1^+), the experimental log ft value is 7.872(11), which matches with shell-model results, i.e., for set I it is 7.314 and for set II it is 8.311. Further, in the ^{215}Bi ($(9/2^-)$) to ^{215}Po ($(11/2_1^+)$) transition at energy 293.53(10) keV, the experimental and shell-model results for set II are in good agreement with each other, i.e., the experimentally log ft value is 6.0(1) while for set I it is 5.349 and for set II it is 5.813. Shell-model results for the allowed transition from ^{214}Bi(1^-) to ^{214}Po(1_1^-) at energy 1994.639(13) keV were also calculated. The shell-model log ft value is 8.126 for both set I and set II, which is close to the experimental log ft value, i.e., 7.522(16). This allowed transition corresponds to the branching fraction of 0.201% in the case of set II using the experimental Q value.

TABLE II. The same as in Table I but for the Bi → Po transitions.

Transition				log ft			$[\overline{C(w_e)}]^{1/2}$		
Initial (J_i^π)	Final (J_f^π)	Decay mode	Energy (keV)	Expt.	Set I	Set II	Expt.	Set I	Set II
^{210}Bi(1^-)	^{210}Po(0_1^+)	1st FNU	0.0	8.0	6.690	8.114	3.062	13.842	2.686
^{211}Bi($9/2^-$)	^{211}Po($9/2_1^+$)	1st FNU	0.0	5.99(2)	6.143	6.140	30.978	25.982	26.053
^{212}Bi($1^{(-)}$)	^{212}Po(0_1^+)	1st FNU	0.0	7.2664(16)	7.330	8.951	7.126	6.621	1.024
	^{212}Po(2_1^+)	1st FNU	727.330(9)	7.720(11)	7.017	7.609	4.227	9.498	4.803
	^{212}Po(2_2^+)	1st FNU	1512.70(8)	7.093(13)	6.554	6.645	8.701	16.179	14.581
	^{212}Po(1_1^+)	1st FNU	1620.738(10)	6.748(11)	6.079	6.384	12.944	27.973	19.679
	^{212}Po(2_3^+)	1st FNU	1679.450(14)	7.51(6)	5.850	6.447	5.383	36.411	18.295
	^{212}Po(0_2^+)	1st FNU	1800.9(2)	8.05(9)	8.103	7.780	2.891	2.721	3.945
	^{212}Po(2_4^+)	1st FNU	1805.96(10)	6.695(21)	6.546	6.926	13.758	16.327	10.543
^{213}Bi($9/2^-$)	^{213}Po($9/2_1^+$)	1st FNU	0.0	6.31(1)	6.367	6.358	21.235	20.068	20.287
	^{213}Po ($(11/2_1^+)$)	1st FNU	292.805(8)	8.45(10)	5.386	5.869	1.910	62.110	35.590
	^{213}Po ($(7/2_1^+)$)	1st FNU	440.446(9)	6.08(1)	9.381	9.302	28.252	0.624	0.684
	^{213}Po ($(5/2_1^+)$)	1st FU	600.87 (17)	10.03(9)	13.513	13.462	0.448	0.005	0.006
	^{213}Po ($(13/2_1^+)$)	1st FU	867.98(3)	8.64(5)	10.457	10.458	1.589	0.181	0.181
	^{213}Po ($(9/2_2^+)$)	1st FNU	1003.605(22)	7.49(3)	6.096	6.091	5.452	27.435	27.586
	^{213}Po ($(9/2_3^+)$)	1st FNU	1045.65(9)	7.85(7)	7.196	7.211	3.640	7.727	7.592
	^{213}Po ($(11/2_2^+)$)	1st FNU	1045.65(9)	7.85(7)	8.293	8.591	3.640	2.184	1.551
^{214}Bi(1^-)	^{214}Po(0_1^+)	1st FNU	0.0	7.872(11)	7.314	8.311	3.586	6.746	2.142
	^{214}Po(2_1^+)	1st FNU	609.318(5)	9.06(7)	7.649	8.318	0.904	4.590	2.124
	^{214}Po(3_1^-)	2nd FNU	1274.765(9)	9.5(3)	11.161	11.542	210.292	31.069	20.037
	^{214}Po(2_2^+)	1st FNU	1377.681(7)	7.374(11)	6.695	6.978	6.296	13.754	9.934
	^{214}Po(0_2^+)	1st FNU	1415.498(8)	8.25(3)	7.380	7.644	2.296	6.250	4.616
	^{214}Po(2_3^+)	1st FNU	1543.370(9)	7.593(12)	6.299	6.926	4.893	21.696	10.548
	^{214}Po(2_4^+)	1st FNU	1661.282(14)	8.21(4)	5.862	6.239	2.405	35.914	23.261
	^{214}Po(2_5^+)	1st FNU	1729.613(7)	6.654(12)	6.506	7.167	14.423	17.094	7.992
	^{214}Po(1_1^+)	1st FNU	1764.520(8)	6.634(13)	6.166	6.381	14.759	25.289	19.754
	^{214}Po(2_6^+)	1st FNU	1847.446(9)	6.859(13)	6.379	6.729	11.391	19.801	13.236
	^{214}Po(1_1^-)	Allowed	1994.639(13)	7.522(16)	8.126	8.126	≈ 0.0	≈ 0.0	≈ 0.0
^{215}Bi ($(9/2^-)$)	^{215}Po($9/2_1^+$)	1st FNU	0.0	>6.9	6.653	6.642	<10.866	14.442	14.619
	^{215}Po($7/2_1^+$)	1st FNU	271.11(10)	>8.2	10.020	8.737	<2.432	0.299	1.312
	^{215}Po ($(11/2_1^+)$)	1st FNU	293.53(10)	6.0(1)	5.349	5.813	30.623	64.770	38.001
	^{215}Po($5/2_1^+$)	1st FU	401.6(10)	7.7	13.796	13.714	4.326	0.004	0.004
	^{215}Po ($(7/2_2^+)$)	1st FNU	517.53(17)	7.8	9.041	8.965	3.855	0.924	1.008
	^{215}Po ($(9/2_2^+)$)	1st FNU	517.53(17)	7.8	6.619	6.608	3.855	15.024	15.20
	^{215}Po ($(11/2_2^+)$)	1st FNU	609.0(5)	7.4	9.058	10.090	6.110	0.905	0.276
	^{215}Po ($(13/2_1^+)$)	1st FU	609.0(5)	7.4	9.931	9.933	6.110	0.332	0.331

Experimentally this value of branching fraction is 1.192(21)%. There are several transitions for which our computations overestimate or underestimate the log ft value. For instance, there are small discrepancies in the results of ^{213}Bi decay. For the transition from ^{213}Bi($9/2^-$) to ^{213}Po ($(5/2_1^+)$) at energy 600.87(17) keV, the experimental log ft value is 10.03(9) whereas the theoretical value for set I is 13.513 and for set II it is 13.462. Also, for the ^{215}Bi ($(9/2^-)$) to ^{215}Po($5/2_1^+$) transition at energy 401.6(10) keV the experimental log ft value is 7.7 while the theoretical value for set I is 13.796 and for set II it is 13.714, which are approximately twice the experimental value. This can be because of several reasons. First, the $9/2^-$ state of ^{215}Bi is not yet confirmed, and second, there are several approximations (such as the impulse approximation) assumed while calculating log ft and half-lives in the shell-model calculations. Further, there are several transitions where unique assignments of spin-parity are not possible. We have calculated shell-model results for all possible spins and parities of the states. However, it is difficult to make unique assignments for these states because their results are in close proximity to each other. For instance, in the case of ^{213}Bi($9/2^-$) to ^{213}Po ($(9/2_3^+)$, $(11/2_2^+)$) at energy 1045.65(9) keV, the experimental log ft value is 7.85(7), and the shell-model results for both $9/2_3^+$ and $11/2_2^+$ in ^{213}Po give values close to the experimental value. Thus, we can not make a unique assignment of spin-parity for the state of ^{213}Po at 1045.65(9) keV.

As Q values play very important roles in the calculation of beta-decay properties, we also calculated theoretical Q values for the concerned nuclei; they are listed in Table III. In this paper, we used experimental Q values for the calculation of shell-model results. Further, for better comparison, we also used theoretical Q values to calculate log ft and

TABLE III. Comparison between the shell-model Q values and experimental [48] Q values.

Transition		E(SM) (MeV)		Q value (MeV)	
Initial	Final	Initial	Final	Expt.	Theoretical
^{210}Pb(0^+)	^{210}Bi(1^-)	−9.091	−8.403	0.0635(5)	0.092
^{211}Pb($9/2^+$)	^{211}Bi($9/2^-$)	−12.936	−13.512	1.367(6)	1.356
^{212}Pb(0^+)	^{212}Bi($1^{(-)}$)	−18.034	−17.882	0.5691(18)	0.628
^{213}Pb (($9/2^+$))	^{213}Bi($9/2^-$)	−21.762	−23.044	2.030(8)	2.062
^{214}Pb(0^+)	^{214}Bi(1^-)	−26.788	−27.149	1.018(11)	1.141
^{215}Pb (($9/2^+$))	^{215}Bi (($9/2^-$))	−30.370	−32.355	2.770(10)	2.765
^{210}Bi(1^-)	^{210}Po(0^+)	−8.403	−8.762	1.1622(8)	1.139
^{211}Bi($9/2^-$)	^{211}Po (($9/2^+$))	−13.512	−13.309	0.574(5)	0.577
^{212}Bi($1^{(-)}$)	^{212}Po(0^+)	−17.882	−19.212	2.2515(17)	2.110
^{213}Bi($9/2^-$)	^{213}Po($9/2^+$)	−23.044	−23.598	1.422(5)	1.334
^{214}Bi(1^-)	^{214}Po(0^+)	−27.149	−29.440	3.269(11)	3.071
^{215}Bi (($9/2^-$))	^{215}Po($9/2^+$)	−32.355	−33.661	2.189(15)	2.086

half-lives of the transitions included in this paper. Columns 1 and 2 show initial and final ground states of the transitions of the concerned nuclei, and columns 3 and 4 show shell-model binding energies of these nuclei. Column 5 shows experimental Q values and column 6 shows calculated shell-model Q values. It can be concluded that these shell-model Q values are in close proximity with the experimental ones. For instance, the theoretical Q value for the ^{215}Pb to ^{215}Bi transition is 2.765 MeV while the experimental value is 2.770(10) MeV. These two values are very close to each other.

Table IV compares theoretical and experimental half-lives for Pb to Bi transitions using both sets of the coupling constants. We calculated half-lives using experimental Q values. Since we know beta-decay half-lives are very sensitive to the Q values, we calculated half-lives using theoretical Q values also. These half-lives were calculated using the property of transition probability that it is additive in nature. It can be concluded from this table that our calculations of half-lives match well with the experimental half-lives in most of the cases. For instance, the experimental half-life value for the ^{211}Pb to ^{211}Bi transition is 36.1(2) min while the theoretical value for set I is 36.052 min with the experimental Q value. In the case of the transition from ^{210}Pb(0^+) to ^{210}Bi, the experimental half-life does not match well with the result of set I but matches well with the result of set II. Minor discrepancies in the results can be explained as there are several transitions for which unique spin-parity assignments are not possible. Therefore, we have to exclude these transitions in our calculations, leading to some deviation in the results.

Table V compares theoretical and experimental half-lives for Bi to Po transitions using both sets of the weak coupling constants. Calculations for half-lives were done using both theoretical and experimental Q values. The theoretical results for the half-lives agree pretty well with the experimental half-lives in most of the cases. For instance, the experimental half-life value for the ^{210}Bi to ^{210}Po transition is 5.012(5) d while the theoretical value for set II is 5.631 d with the experimental Q value and it comes out to be 5.894 d with the theoretical Q value.

For better comparison of half-lives, we have plotted calculated and experimental half-lives, with the use of both the experimental and shell-model Q values, in Fig. 2 on a logarithmic scale for Pb to Bi transitions. This plot shows half-lives for both sets of the weak coupling constants using both experimental and theoretical Q values. It can be concluded from Fig. 2 that set II with the experimental Q values

TABLE IV. Comparison between theoretical and experimental [48] half-lives values for Pb → Bi transitions for experimental and theoretical Q values. The calculations are carried out through two sets of quenching factors in the weak coupling constants g_V and g_A. The values of quenching factor are for set I $(g_A/g_A^{free}, g_V/g_V^{free}) = (0.38, 1.00)$ and for set II $(g_A/g_A^{free}, g_V/g_V^{free}) = (0.38, 0.51)$. The quenching factors of set I were calculated from this work and those of set II were taken from [27].

Transition		Half-life				
Initial	Final	Expt.	Set I (Expt. Q)	Set I (Theor. Q)	Set II (Expt. Q)	Set II (Theor. Q)
^{210}Pb(0^+)	^{210}Bi	22.20(22) yr	5.974 yr	0.886 yr	23.087 yr	1.350 yr
^{211}Pb($9/2^+$)	^{211}Bi	36.1(2) min	36.052 min	40.534 min	41.743 min	43.157 min
^{212}Pb(0^+)	^{212}Bi	10.622(7) h	8.804 h	4.069 h	11.004 h	4.476 h
^{213}Pb (($9/2^+$))	^{213}Bi	10.2(3) min	15.452 min	16.246 min	19.542 min	18.661 min
^{214}Pb(0^+)	^{214}Bi	27.06(7) min	10.733 min	10.558 min	33.306 min	33.792 min
^{215}Pb (($9/2^+$))	^{215}Bi	147 s	617.223 s	675.112 s	3486.387 s	813.294 s

TABLE V. The same as in Table IV but for the Bi → Po transitions.

Transition		Half-life				
Initial	Final	Expt.	Set I (Expt. Q)	Set I (Theor. Q)	Set II (Expt. Q)	Set II (Theor. Q)
^{210}Bi(1^-)	^{210}Po	5.012(5) d	0.212 d	0.227 d	5.631 d	5.894 d
^{211}Bi($9/2^-$)	^{211}Po	2.14 (2) min	2.769 min	2.750 min	2.754 min	2.736 min
^{212}Bi($1^{(-)}$)	^{212}Po	60.55(6) min	56.694 min	79.610 min	297.021 min	466.002 min
^{213}Bi($9/2^-$)	^{213}Po	45.59(6) min	13.461 min	27.040 min	28.880 min	49.984 min
^{214}Bi(1^-)	^{214}Po	19.71(2) min	4.261 min	7.786 min	12.033 min	23.224 min
^{215}Bi (($9/2^-$))	^{215}Po	7.6(2) min	2.103 min	3.409 min	5.275 min	8.152 min

matches extremely well with the experimental half-lives up to $N = 130$. Further, at $N = 131$, there is a good agreement between the experimental half-lives and those obtained for set I with both the experimental and theoretical Q values. There is a slight deviation at $N = 133$. However, set I using both the experimental and theoretical Q values approaches the experimental value significantly better than the others.

In Fig. 3, half-lives have been plotted for Bi to Pb transitions for both sets of the weak coupling constants using both Q values. For $N = 127$ and 128, results of set II obtained with experimental and theoretical Q values agree very well with the experimental results. However, set I using experimental Q values is more favorable than the others at $N = 129$, while there is a good agreement between the experimental values and set II values for both theoretical and experimental Q values at $N = 130$ to 132.

For a better and more detailed comparison of the shell-model and experimental half-lives, we calculated the error in the theoretical half-lives compared to the experimental ones. Table VI shows the deviation in calculated half-lives compared to the experimental half-lives on a logarithmic scale because the magnitudes of half-lives listed in Tables IV and V vary in a wide range. Therefore in this table we have tried to show the mean deviation and fluctuation [49–51] from the experimental data on a logartihmic scale for both sets of the weak coupling constants, including both theoretical and experimental Q values. Here, r is the measure of deviation, which is defined as

$$r = \log_{10}\left(T_{1/2}^{\mathrm{Calc}}/T_{1/2}^{\mathrm{exp}}\right), \tag{22}$$

where $T_{1/2}^{\mathrm{Calc}}$ is the theoretically calculated half-life value and $T_{1/2}^{\mathrm{exp}}$ is the experimental half-life value. Its mean value is denoted by $\bar{r}$ and standard deviation is denoted by σ. These quantities are defined as

$$\bar{r} = \frac{1}{n}\sum_{i=1}^{n} r_i, \tag{23}$$

$$\sigma = \left[\frac{1}{n}\sum_{i=1}^{n}(r_i - \bar{r})^2\right]^{1/2}, \tag{24}$$

where n is the number of transitions taken to calculate the half-lives and the index i goes from 1 to n. In these calculations, the

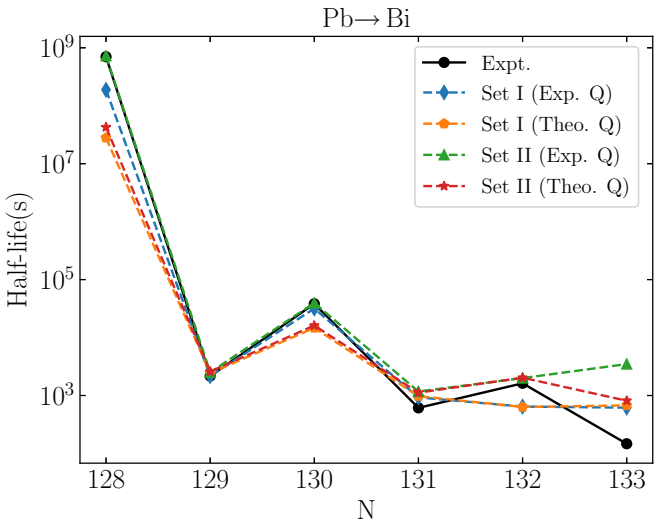

FIG. 2. Comparison of calculated and experimental [48] half-lives for allowed and first-forbidden transitions for Pb → Bi with experimental and shell-model Q values. For set I $(g_A/g_A^{\mathrm{free}}, g_V/g_V^{\mathrm{free}}) = (0.38, 1.00)$ and for set II $(g_A/g_A^{\mathrm{free}}, g_V/g_V^{\mathrm{free}}) = (0.38, 0.51)$ were used.

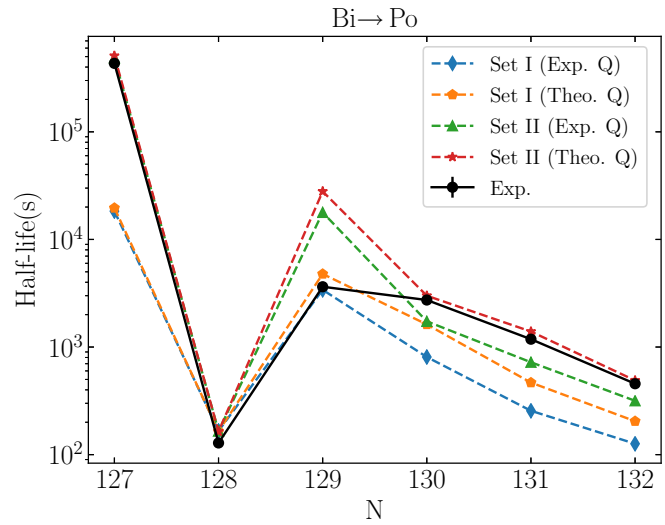

FIG. 3. Comparison of calculated and experimental [48] half-lives for allowed and first-forbidden transitions for Bi → Po with experimental and shell-model Q values. For set I $(g_A/g_A^{\mathrm{free}}, g_V/g_V^{\mathrm{free}}) = (0.38, 1.00)$ and for set II $(g_A/g_A^{\mathrm{free}}, g_V/g_V^{\mathrm{free}}) = (0.38, 0.51)$ were used.

TABLE VI. Error in calculated half-life values in comparison to experimental [48] half-lives. Comparison is given for both sets of the weak coupling constants using both experimental and shell-model Q values.

	Using Q (Expt.)		Using Q (Theor.)	
	Set I	Set II	Set I	Set II
$\bar{r}$	−0.274	0.177	−0.284	0.066
σ	0.487	0.431	0.577	0.486
$10^{\bar{r}}$	0.532	1.503	0.520	1.164
10^{σ}	3.069	2.701	3.780	3.059

value of n is 12. The mean error value and standard deviation should be equal to zero for minimal deviations because we have calculated them on a logarithmic scale. Our results are approaching zero for both experimental and theoretical Q values, so we can conclude that our calculations show good agreement with the experimental data. Use of experimental Q values is generally better than the case of theoretical Q values. Use of set II improves the agreement with the experimental data compared with set I. We have also shown the mean and standard deviation in powers of 10 to eliminate the logarithmic scale.

Recently, a new beta-decaying isomeric state (8^-) for ^{214}Bi^m was predicted at the CERN-ISOLDE facility, decaying to various excited states of ^{214}Po listed in Table VII with a half-life of 9.39(10) min. In Ref. [29], experimental energy spectra are compared with shell-model results, but shell-model results for beta-decay properties such as $\log ft$ are not reported. We here give theoretical estimates for these results. Table VII shows the $\log ft$ and average shape factor for the ^{214}Bi $((8^-))$ isomer. Computations were carried out for various transitions from the ^{214}Bi $((8^-))$ isomer to different excited states of ^{214}Po by using theoretical Q values. All the transitions in this table are first forbidden nonunique transitions except one transition that is a first forbidden unique transition. Thus, we have compared our shell-model results according to the decay mode with the experimental data available in the reference mentioned above. Good results are obtained for the shell-model calculations. For instance, at excitation energy 1584.4(4) keV for a transition from ^{214}Bi $((8^-))$ to ^{214}Po $((8^+_1))$, the experimental $\log ft$ value is 6.25(12) and the theoretical values are 6.264 for set I and 6.255 for set II. We computed $\log ft$ values for all the transitions where more than one spin-parity assignment is possible. Based on shell-model results it is possible to predict one suitable spin-parity for the state at that energy level. It can be inferred that the spin-parity for the state at energy 1633.5(4) keV can be 8^+_2 because its theoretical $\log ft$ values are 6.466 for set I and 6.518 for set II, which are close to the experimental value, i.e., 6.62(14). Also, at energy level 1843.0(4) keV, the experimental $\log ft$ will be decided based on whether the decay is unique first forbidden or nonunique first forbidden beta decay. As a result, the state is predicted to be 7^+_1 out of two possible spin-parity states, 6^+_1 and 7^+_1, because the calculated $\log ft$ value of the 7^+_1 state is close to the experimental value as compared to that for 6^+_1. At energy level 1969.1(4) keV, it is difficult to assign a unique spin-parity for the state out of two 8^+_4 and 9^+_2 states, because both spin-parity assignments give good results. At energy 2059.5(4) keV, 8^+_5 can be suitable as its $\log ft$ value for set I is 6.771 and for set II it is 7.558, whereas its experimental value is 6.04(13). Also, at energy 2197.6(4) keV, the 8^+_6 state can be predicted because its theoretical $\log ft$ value is 7.297 and the experimental value is 6.40(14).

IV. CONCLUSION

In the present work, we calculated various beta-decay properties such as $\log ft$ values, shape factors, and half-lives

TABLE VII. Comparison between theoretical and experimental [29] $\log ft$ values for ^{214}Bi^m $((8^-))$ transitions to the different excited states in ^{214}Po transitions. The calculations are carried out through two sets of quenching factors in the weak coupling constants g_V and g_A. The values of quenching factors are for set I $(g_A/g_A^{free}, g_V/g_V^{free}) = (0.38, 1.00)$ and for set II $(g_A/g_A^{free}, g_V/g_V^{free}) = (0.38, 0.51)$. The quenching factors of set I were calculated from this work and those of set II were taken from [27].

Final state				$\log ft$			$[\overline{C(w_e)}]^{1/2}$		
J^π_f (Expt.)	J^π_f (SM)	Decay mode	Energy (keV)	Expt.	Set I	Set II	Expt.	Set I	Set II
(8^+)	8^+_1	1st FNU	1584.4(4)	6.25(12)	6.264	6.255	22.964	22.587	22.834
$(8^+, 9^+)$	8^+_2	1st FNU	1633.5(4)	6.62(14)	6.466	6.518	14.999	17.917	16.867
$(8^+, 9^+)$	9^+_1	1st FNU	1633.5(4)	6.62(14)	5.468	5.941	14.999	56.523	32.786
(8^+)	8^+_3	1st FNU	1824.5(4)	6.25(12)	5.945	6.018	22.964	32.607	30.006
$(6^+, 7^+)$	6^+_1	1st FU	1843.0(4)	8.69(17)	11.130	11.147	1.384	0.083	0.082
$(6^+, 7^+)$	7^+_1	1st FNU	1843.0(4)	7.86(13)	9.643	8.726	3.598	0.462	1.328
$(8^+, 9^+)$	8^+_4	1st FNU	1969.1(4)	6.93(13)	6.371	6.757	10.497	19.973	12.813
$(8^+, 9^+)$	9^+_2	1st FNU	1969.1(4)	6.93(13)	7.005	7.517	10.497	9.631	5.341
$(8^+, 9^+)$	8^+_5	1st FNU	2059.5(4)	6.04(13)	6.771	7.558	29.245	12.610	5.096
$(8^+, 9^+)$	9^+_3	1st FNU	2059.5(4)	6.04(13)	10.183	10.148	29.245	0.248	0.258
(9)	9^+_4	1st FNU	2159.0(4)	7.80(16)	7.743	7.895	3.855	4.118	3.454
$(8^+, 9^+)$	8^+_6	1st FNU	2197.6(4)	6.40(14)	7.297	7.297	19.322	6.877	6.883
$(8^+, 9^+)$	9^+_5	1st FNU	2197.6(4)	6.40(14)	8.372	9.657	19.322	1.995	0.455

of nuclei in the region northeast of ^{208}Pb nucleus. These computations were performed for $^{210–215}$Pb $\rightarrow$ $^{210–215}$Bi and $^{210–215}$Bi $\rightarrow$ $^{210–215}$Po transitions using the KHPE effective interaction without any truncation. First, we computed the quenching factor using the chi-square fitting method. Then, using this value of the quenching factor and another set taken from Ref. [27], we calculated log ft, shape factors, and half-lives of these transitions. We also calculated shell-model Q values of the concerned nuclei, and used both experimental and theoretical Q values to study these beta-decay properties for better comparison. Our results for the log ft values and half-lives obtained by the shell-model calculations show good agreement with the available experimental data. Use of experimental Q values and inclusion of the quenching in both the axial and vector couplings is generally better compared with the case of theoretical Q values and the quenching in the axial coupling only. We have also calculated log ft values for the ^{214}Bi^m ((8^-)) isomer recently predicted at the CERN-ISOLDE facility. We used shell-model Q values for these calculations. We also confirmed spins and parities of various states with the help of shell-model calculations, where unique assignments of spin-parity are not possible experimentally. Also, we calculated log ft values of the transitions whose experimental data are not available. These shell-model results will add more information to the present data and will be very helpful for future experiments. Further, shell-model results can be improved with the inclusion of core polarization effects [23] by allowing nucleon excitation across the ^{208}Pb core and tuning effective interactions.

ACKNOWLEDGMENTS

S.S. would like to thank CSIR-HRDG (India) for financial support for her Ph.D. thesis work. P.C.S. acknowledges a research grant from SERB (India), No. CRG/2019/000556. T.S. acknowledges JSPS (Japan) for JSPS KAKENHI Grant No. JP19K03855.

APPENDIX

1. The quantities $M_K(k_e, k_\nu)$ and $m_K(k_e, k_\nu)$

Here, we have introduced $M_K(k_e, k_\nu)$ and $m_K(k_e, k_\nu)$ in order to obtain the final expression of the shape factor in Eq. (8). As in the earlier works [11,12,34,47,52], we have included the next-to-leading order (NLO) corrections to the shape factor. In this way, the number of NMEs increases drastically, and, in the case of the second-forbidden nonunique β^- decay, the number of NMEs is increased from 8 to 27 (see the full details about the NLO corrections in Refs. [34,47]). The explicit expressions of the quantities $M_K(k_e, k_\nu)$ and $m_K(k_e, k_\nu)$ can be expressed in the following way (also see Ref. [34]) that includes both the leading order and next-to-leading order corrections in the shape factor.

(1) In the case of the summation $k_e + k_\nu = K + 1$, the quantity $M(k_e, k_\nu)$ is given by

$$
\begin{aligned}
M_K(k_e,k_\nu) = {} & \mathcal{K}_K \xi^{k_e+k_\nu-2}\left(\sqrt{w_e^2-1}\right)^{k_e-1}(w_0-w_e)^{k_\nu-1}\times\Bigg[\sqrt{\frac{2K+1}{K}}R^{-(K-1)}g_{\rm V}\,{}^{V}\mathcal{M}^{(0)}_{KK-11} \\
& -\left(\frac{w_e}{2k_e+1}+\frac{w_0-w_e}{2k_\nu+1}\right)\xi R^{-K}g_{\rm V}\,{}^{V}\mathcal{M}^{(0)}_{KK0}-\frac{\alpha Z}{2k_e+1}R^{-K}g_{\rm V}\,{}^{V}\mathcal{M}^{(0)}_{KK0}(k_e,1,1,1) \\
& +\sqrt{\frac{K+1}{K}}\left(\frac{w_e}{2k_e+1}-\frac{w_0-w_e}{2k_\nu+1}\right)\xi R^{-K}g_{\rm A}\,{}^{A}\mathcal{M}^{(0)}_{KK1}+\sqrt{\frac{K+1}{K}}\frac{\alpha Z}{2k_e+1}R^{-K}g_{\rm A}\,{}^{A}\mathcal{M}^{(0)}_{KK1}(k_e,1,1,1) \\
& -2\sqrt{\frac{K+1}{2K+1}}\frac{w_e}{2k_e+1}\frac{w_0-w_e}{2k_\nu+1}\xi^2R^{-(K+1)}g_{\rm V}\,{}^{V}\mathcal{M}^{(0)}_{KK+11}-2\sqrt{\frac{K+1}{2K+1}}\frac{\alpha Z}{2k_e+1}\frac{w_0-w_e}{2k_\nu+1}\xi R^{-(K+1)}g_{\rm V} \\
& \times\,{}^{V}\mathcal{M}^{(0)}_{KK+11}(k_e,1,1,1)+\frac{1}{\sqrt{K(2K+1)}}\frac{w_e}{2k_e+1}\frac{w_0-w_e}{2k_\nu+1}\xi^2R^{-(K-1)}g_{\rm V}\,{}^{V}\mathcal{M}^{(1)}_{KK-11} \\
& +\frac{1}{2}\sqrt{\frac{2K+1}{K}}\left(\frac{1}{2k_e+1}-\frac{w_e^2}{2k_e+1}-\frac{(w_0-w_e)^2}{2k_\nu+1}\right)\xi^2R^{-(K-1)}g_{\rm V}\,{}^{V}\mathcal{M}^{(1)}_{KK-11} \\
& +\frac{1}{\sqrt{K(2K+1)}}\frac{\alpha Z}{2k_e+1}\frac{w_0-w_e}{2k_\nu+1}\xi R^{-(K-1)}g_{\rm V}\,{}^{V}\mathcal{M}^{(1)}_{KK-11}(k_e,1,1,1)-\sqrt{\frac{2K+1}{K}}\frac{\alpha Z w_e}{2k_e+1}\xi R^{-(K-1)}g_{\rm V} \\
& \times\,{}^{V}\mathcal{M}^{(1)}_{KK-11}(k_e,2,2,1)-\frac{1}{2}\sqrt{\frac{2K+1}{K}}\frac{(\alpha Z)^2}{2k_e+1}R^{-(K-1)}g_{\rm V}\,{}^{V}\mathcal{M}^{(1)}_{KK-11}(k_e,2,2,2)\Bigg], \qquad \text{(A1)}
\end{aligned}
$$

and the quantity $m(k_e, k_\nu)$ is given by

$$
\begin{aligned}
m_K(k_e,k_\nu) = {} & \mathcal{K}_K \xi^{k_e+k_\nu-1}\left(\sqrt{w_e^2-1}\right)^{k_e-1}(w_0-w_e)^{k_\nu-1}\frac{1}{2k_e+1}\Bigg[-R^{-K}g_{\rm V}\,{}^{V}\mathcal{M}^{(0)}_{KK0}+\sqrt{\frac{K+1}{K}}R^{-K}g_{\rm A}\,{}^{A}\mathcal{M}^{(0)}_{KK1} \\
& -2\sqrt{\frac{K+1}{2K+1}}\frac{w_0-w_e}{2k_\nu+1}\xi R^{-(K+1)}g_{\rm V}\,{}^{V}\mathcal{M}^{(0)}_{KK+11}
\end{aligned}
$$

$$+\frac{1}{\sqrt{K(2K+1)}}\frac{w_0-w_e}{2k_\nu+1}\xi R^{-(K-1)}g_{\rm V}{}^{V}\mathcal{M}^{(1)}_{KK-11}$$
$$-\frac{1}{2}\sqrt{\frac{2K+1}{K}}\alpha Z R^{-(K-1)}g_{\rm V}{}^{V}\mathcal{M}^{(1)}_{KK-11}(K_e,2,1,1)\Bigg]. \tag{A2}$$

(2) In the case of the summation $k_e+k_\nu=K+2$, the quantities are given by

$$M_K(k_e,k_\nu)=\tilde{\mathcal{K}}_K\xi^{k_e+k_\nu-2}(\sqrt{w_e^2-1})^{k_e-1}(w_0-w_e)^{k_\nu-1}\sqrt{\frac{K+1}{(2k_e-1)(2k_\nu-1)}}\Bigg[R^{-K}g_{\rm V}{}^{V}\mathcal{M}^{(0)}_{KK0}+\frac{k_e-k_\nu}{\sqrt{K(K+1)}}$$
$$\times R^{-K}g_{\rm A}{}^{A}\mathcal{M}^{(0)}_{KK1}+\sqrt{\frac{1}{(K+1)(2K+1)}}\left(\frac{2k_e-1}{2k_e+1}w_e+\frac{2k_\nu-1}{2k_\nu+1}(w_0-w_e)\right)\xi R^{-(K+1)}g_{\rm V}{}^{V}\mathcal{M}^{(0)}_{KK+11}$$
$$+\sqrt{\frac{1}{(K+1)(2K+1)}}\frac{2k_e-1}{2k_e+1}\alpha Z^{-(K+1)}g_{\rm V}{}^{V}\mathcal{M}^{(0)}_{KK+11}(k_e,1,1,1)$$
$$+\sqrt{\frac{1}{K(2K+1)}}\left(\frac{2(k_\nu-1)}{2k_e+1}w_e+\frac{2(k_e-1)}{2k_\nu+1}(w_0-w_e)\right)\xi R^{-(K-1)}g_{\rm V}{}^{V}\mathcal{M}^{(1)}_{KK-11}$$
$$+\sqrt{\frac{1}{K(2K+1)}}\frac{2(k_\nu-1)}{2k_e+1}\alpha Z R^{-(K-1)}g_{\rm V}{}^{V}\mathcal{M}^{(1)}_{KK-11}(k_e,1,1,1)\Bigg] \tag{A3}$$

and

$$m_K(k_e,k_\nu)=\tilde{\mathcal{K}}_K\xi^{k_e+k_\nu-1}(\sqrt{w_e^2-1})^{k_e-1}(w_0-w_e)^{k_\nu-1}\sqrt{\frac{K+1}{(2k_e-1)(2k_\nu-1)}}\frac{1}{2k_e+1}\Bigg[\sqrt{\frac{1}{(K+1)(2K+1)}}$$
$$\times(2k_e-1)R^{-(K+1)}g_{\rm V}{}^{V}\mathcal{M}^{(0)}_{KK+11}+2\sqrt{\frac{1}{K(2K+1)}}(k_\nu-1)R^{-K}g_{\rm A}{}^{A}\mathcal{M}^{(1)}_{KK1}\Bigg]. \tag{A4}$$

In addition to Eqs (A3) and (A4), one additional term $M_{K+1}(k_e,k_\nu)$ is also included in the shape factor for the summation $k_e+k_\nu=K+2$, which is given by

$$M_{K+1}(k_e,k_\nu)=\tilde{\mathcal{K}}_K\xi^{k_e+k_\nu-2}(\sqrt{w_e^2-1})^{k_e-1}(w_0-w_e)^{k_\nu-1}\Bigg[-R^{-K}g_{\rm A}{}^{A}\mathcal{M}^{(0)}_{K+1K1}$$
$$+\sqrt{\frac{K+1}{2K+3}}\left(\frac{w_e}{2k_e+1}+\frac{w_0-w_e}{2k_\nu+1}\right)\xi R^{-(K+1)}g_{\rm A}{}^{A}\mathcal{M}^{(0)}_{K+1K+10}$$
$$+\sqrt{\frac{K+1}{2K+3}}\frac{\alpha Z}{2k_e+1}R^{-(K+1)}g_{\rm A}{}^{A}\mathcal{M}^{(0)}_{K+1K+10}(k_e,1,1,1)$$
$$-\sqrt{\frac{K+2}{2K+3}}\left(\frac{w_e}{2k_e+1}-\frac{w_0-w_e}{2k_\nu+1}\right)\xi R^{-(K+1)}g_{\rm V}{}^{V}\mathcal{M}^{(0)}_{K+1K+11}$$
$$-\sqrt{\frac{K+2}{2K+3}}\frac{\alpha Z}{2k_e+1}R^{-(K+1)}g_{\rm V}{}^{V}\mathcal{M}^{(0)}_{K+1K+11}(k_e,1,1,1)\Bigg], \tag{A5}$$

where the auxiliary quantity $\xi=m_ec^2R/(\hbar c)$ and the prefactors $\mathcal{K}_K$ and $\tilde{\mathcal{K}}_K$ in Eqs. (A1)–(A5) are expressed as

$$\mathcal{K}_K=\sqrt{\frac{1}{2}}\sqrt{\frac{(2K)!!}{(2K+1)!!}}\sqrt{\frac{1}{(2k_e-1)!(2k_\nu-1)!}}, \tag{A6}$$

$$\tilde{\mathcal{K}}_K=\sqrt{\frac{(2K)!!}{(2K+1)!!}}\sqrt{\frac{1}{(2k_e-1)!(2k_\nu-1)!}}, \tag{A7}$$

where the NMEs ${}^{V/A}\mathcal{M}^{(N)}_{KLS}(k_e,m,n,\rho)$ contains all the nuclear-structure information of the nuclear β decay transitions, and these are discussed in the next section.

2. Nuclear matrix elements

To calculate the Eq. (13), we need the corresponding SPMEs that comes from the β decay transition operator between the initial and final single-particle wave functions:

$$ {}^{V}m^{(N)}_{KLS}(pn)(k_e,m,n,\rho) = \frac{1}{\hat{K}}\left(p\left\|T_{KLS}\left(\frac{r}{R}\right)^{2N}\mathcal{I}(k_e,m,n,\rho;r)\right\|n\right), \tag{A8} $$

$$ {}^{A}m^{(N)}_{KLS}(pn)(k_e,m,n,\rho) = \frac{1}{\hat{K}}\left(p\left\|\gamma_5 T_{KLS}\left(\frac{r}{R}\right)^{2N}\mathcal{I}(k_e,m,n,\rho;r)\right\|n\right), \tag{A9} $$

Inside the NMEs, the coefficients $\mathcal{I}(k_e,m,n,\rho;r)$ are a function of r and depend on the nuclear charge distribution. More information on these coefficients is found in Ref. [35]. The T_{KLS} is the transition operator, which is defined as

$$ T_{KLS} = \begin{cases} i^L r^L Y_{LM}\delta_{LK}, & S=0, \\ i^L r^L (-1)^{L-K+1} r^L [Y_L\boldsymbol{\sigma}]_{KM}, & S=1, \end{cases} \tag{A10} $$

where Y_{LM} are spherical harmonics functions and $\boldsymbol{\sigma}$ is the Pauli matrix.

In Eqs. (A1)–(A5), the required all NMEs can be obtained from only four kinds of single-particle matrix elements, which are the vector or axial-vector character. Now we define the single-particle expression for all the nuclear matrix elements for Eq. (13):

$$ \begin{aligned} {}^{V}m^{(N)}_{KK0}(k_e,m,n,\rho) = \sqrt{\frac{2}{2J_i+1}}\Bigg\{ & G_{KK0}(k_f,k_i)\int_0^\infty g_f(r,k_f)\left(\frac{r}{R}\right)^{2N+K}\mathcal{I}(k_e,m,n,\rho;r) \\ & \times g_i(r,k_i)r^2dr + \mathrm{sgn}(k_f)\mathrm{sgn}(k_i)G_{KK0}(-k_f,-k_i) \\ & \times \int_0^\infty f_f(r,k_f)\left(\frac{r}{R}\right)^{2N+K}\mathcal{I}(k_e,m,n,\rho;r)f_i(r,k_i)r^2dr\Bigg\}, \end{aligned} \tag{A11a} $$

$$ \begin{aligned} {}^{A}m^{(N)}_{KL1}(k_e,m,n,\rho) = \sqrt{\frac{2}{2J_i+1}}\Bigg\{ & G_{KL1}(k_f,k_i)\int_0^\infty g_f(r,k_f)\left(\frac{r}{R}\right)^{2N+L}\mathcal{I}(k_e,m,n,\rho;r) \\ & \times g_i(r,k_i)r^2dr + \mathrm{sgn}(k_f)\mathrm{sgn}(k_i)G_{KL1}(-k_f,-k_i) \\ & \times \int_0^\infty f_f(r,k_f)\left(\frac{r}{R}\right)^{2N+L}\mathcal{I}(k_e,m,n,\rho;r)f_i(r,k_i)r^2dr\Bigg\}, \end{aligned} \tag{A11b} $$

$$ \begin{aligned} {}^{V}m^{(N)}_{KL1}(k_e,m,n,\rho) = \sqrt{\frac{2}{2J_i+1}}\Bigg\{ & \mathrm{sgn}(k_i)G_{KL1}(k_f,-k_i)\int_0^\infty g_f(r,k_f)\left(\frac{r}{R}\right)^{2N+L} \\ & \times \mathcal{I}(k_e,m,n,\rho;r)f_i(r,k_i)r^2dr + \mathrm{sgn}(k_f)G_{KL1}(-k_f,k_i) \\ & \times \int_0^\infty f_f(r,k_f)\left(\frac{r}{R}\right)^{2N+L}\mathcal{I}(k_e,m,n,\rho;r)g_i(r,k_i)r^2dr\Bigg\}, \end{aligned} \tag{A11c} $$

$$ \begin{aligned} {}^{A}m^{(N)}_{KK0}(k_e,m,n,\rho) = \sqrt{\frac{2}{2J_i+1}}\Bigg\{ & \mathrm{sgn}(k_i)G_{KK0}(k_f,-k_i)\int_0^\infty g_f(r,k_f)\left(\frac{r}{R}\right)^{2N+K} \\ & \times \mathcal{I}(k_e,m,n,\rho;r)f_i(r,k_i)r^2dr + \mathrm{sgn}(k_f)G_{KK0}(-k_f,k_i) \\ & \times \int_0^\infty f_f(r,k_f)\left(\frac{r}{R}\right)^{2N+K}\mathcal{I}(k_e,m,n,\rho;r)g_i(r,k_i)r^2dr\Bigg\}, \end{aligned} \tag{A11d} $$

where $g_i(r,k)/f_i(r,k)$ and $g_f(r,k)/f_f(r,k)$ are the radial wave functions for the initial and final states, respectively and the quantity $G_{KLS}(k_1,k_2)$ is defined in [53] as

$$ \begin{aligned} G_{KLS}(k_1,k_2) = & \sqrt{(2S+1)(2K+1)(2l_1+1)(2l_2+1)(2j_1+1)(2j_2+1)} \\ & \times i^{l_1+l_2+L}(-1)^{(j_1-j_2)}\langle l_1 l_2 00|L0\rangle \begin{Bmatrix} K & S & L \\ j_1 & \frac{1}{2} & l_1 \\ j_2 & \frac{1}{2} & l_2 \end{Bmatrix}. \end{aligned} \tag{A12} $$

The above equations (A11a)–(A11d) are written in the Biedenhan-Rose phase convention [31].

To evaluate the above single-particle matrix elements of (A8) and (A9), we used the relativistic single-particle spinor wave functions [34] for initial and final states, that are given by

$$\phi_{nljm}(\boldsymbol{r}) = \begin{bmatrix} \mathcal{G}_{nljm}(\boldsymbol{r}) \\ \mathcal{F}_{nljm}(\boldsymbol{r}) \end{bmatrix}, \tag{A13}$$

where the large component $\mathcal{G}_{nljm}(\boldsymbol{r})$ is taken as a solution of the nonrelativistic Schrödinger equation for a harmonic oscillator, which is defined as

$$\mathcal{G}_{nljm}(\boldsymbol{r}) = i^L g_{nl}(r)[Y_l \chi_{1/2}]_{jm}, \tag{A14}$$

and here $\chi_{1/2}$ is the nonrelativistic spinor of spin $\frac{1}{2}$. The small component of (A13) is

$$\begin{aligned} \mathcal{F}_{nljm}(\boldsymbol{r}) &= \frac{\boldsymbol{\sigma}.\boldsymbol{p}}{2M_{\mathrm{N}}c}\mathcal{G}_{nljm}(\boldsymbol{r}) \\ &= \frac{i^{l+1}\hbar}{2M_{\mathrm{N}}cb}(-1)^{l+j-\frac{1}{2}}\left[\frac{r}{b}g_{nl}(r) - 2\sqrt{n+j+1}\,g_{nl+1}(r)\right][Y_{l+1}\chi_{1/2}]_{jm}, \end{aligned} \tag{A15}$$

where the $M_{\mathrm{N}} = 940$ MeV$/c$ is the nuclear mass and b is the harmonic-oscillator size parameter. The final expression of the above equation is the analytic form of the $\mathcal{F}_{nljm}$ when g_{nl} is taken to be a harmonic-oscillator wave function.

3. First forbidden nonunique β^- decay with $\Delta J = 0$

In the case of the first forbidden nonunique β^- transitions with zero angular momentum change, i.e., $K = 1$ and $\Delta J = 0$, the shape factor of Eq. (8) is expanded with two more nuclear matrix elements. The additional part of the shape factor is expressed as

$$\begin{aligned} C(w_e) = \zeta^2 g_{\mathrm{A}}^2 \Bigg[&\left(\frac{1}{\zeta}\,{}^A\mathcal{M}^{(0)}_{000} + \frac{w_0}{3}\,{}^A\mathcal{M}^{(0)}_{011} - \frac{\tilde{\alpha}Z}{3}\,{}^A\mathcal{M}^{(0)}_{011}(k_e,1,1,1)\right)^2 + \left(\frac{{}^A\mathcal{M}^{(0)}_{011}}{3}\right)^2 \\ &- \frac{2\gamma_1}{w_e}\left(\frac{1}{\zeta}\,{}^A\mathcal{M}^{(0)}_{000} + \frac{w_0}{3}\,{}^A\mathcal{M}^{(0)}_{011} - \frac{\tilde{\alpha}Z}{3}\,{}^A\mathcal{M}^{(0)}_{011}(k_e,1,1,1)\right)\left(\frac{{}^A\mathcal{M}^{(0)}_{011}}{3}\right)\Bigg], \end{aligned} \tag{A16}$$

where the auxiliary quantities are $\zeta = m_e c^2/\hbar c$ and $\tilde{\alpha}Z = \alpha Z/\xi$. The new matrix elements are now expressed as

$${}^A\mathcal{M}^{(0)}_{000} = \frac{\sqrt{4\pi}}{\hat{j}_i}\sum_{pn} {}^A m^{(0)}_{000}(pn)(\Psi_f \| [c_p^\dagger \tilde{c}_n]_0 \| \Psi_i), \tag{A17}$$

$${}^A\mathcal{M}^{(0)}_{011} = \frac{\sqrt{4\pi}}{\hat{j}_i}\sum_{pn} {}^A m^{(0)}_{011}(pn)(\Psi_f \| [c_p^\dagger \tilde{c}_n]_0 \| \Psi_i). \tag{A18}$$

[1] J. J. Cowan, F. K. Thielemann, and J. W. Truran, The *r*-process and nucleochronology, Phys. Rep. **208**, 267 (1991).

[2] S. Wanajo and Y. Ishimaru, *r*-process calculations and Galactic chemical evolution, Nucl. Phys. A **777**, 676 (2006).

[3] F.-K. Thielemann, M. Eichler, I. V. Panov, and B. Wehmeyer, Neutron star mergers and nucleosynthesis of heavy elements, Annu. Rev. Nucl. Part. Sci. **67**, 253 (2017).

[4] M. Arnould, S. Goriely, and K. Takahashi, The *r*-process of stellar nucleosynthesis: Astrophysics and nuclear physics achievements and mysteries, Phys. Rep. **450**, 97 (2007).

[5] E. M. Burbidge, G. R. Burbidge, W. A. Fowler, and F. Hoyle, Synthesis of the elements in stars, Rev. Mod. Phys. **29**, 547 (1957).

[6] A. G. W. Cameron, Nuclear reactions in stars and nucleogenesis, Pub. Astron. Soc. Pacific **69**, 201 (1957).

[7] S. E. Woosley *et al.*, The r-process and neutrino-heated supernova ejecta, Astrophys. J. **433**, 229 (1994).

[8] T. Suzuki, T. Yoshida, T. Kajino, and T. Otsuka, β decays of isotones with neutron magic number of $N = 126$ and *r*-process nucleosynthesis, Phys. Rev. C **85**, 015802 (2012).

[9] R. J. Carroll *et al.*, Competition between Allowed and First-Forbidden β Decay: The Case of ^{208}Hg$\rightarrow{}^{208}$Tl, Phys. Rev. Lett. **125**, 192501 (2020).

[10] M. Brunet *et al.*, Competition between allowed and first-forbidden β decays of ^{208}At and expansion of the ^{208}Po level scheme, Phys. Rev. C **103**, 054327 (2021).

[11] J. Kostensalo, M. Haaranen, and J. Suhonen, Electron spectra in forbidden β decays and the quenching of the weak axial-vector coupling constant g_A, Phys. Rev. C **95**, 044313 (2017).

[12] J. Kostensalo and J. Suhonen, g_A-driven shapes of electron spectra of forbidden β decays in the nuclear shell-model, Phys. Rev. C **96**, 024317 (2017).

[13] A. Kumar and P. C. Srivastava, Shell-model description for the first-forbidden β^- decay of ^{207}Hg into the one-proton-hole nucleus ^{207}Tl, Nucl. Phys. A **1014**, 122255 (2021).

[14] K. Takahashi, M. Yamada, and T. Kondoh, Beta-decay half-lives calculated on the gross theory, At. Data Nucl. Data Tables **12**, 101 (1973).

[15] I. N. Borzov and S. Goriely, Weak interaction rates of neutron-rich nuclei and the *r*-process nucleosynthesis, Phys. Rev. C **62**, 035501 (2000).

[16] K. Nomura, R. Rodríguez-Guzmán, and L. M. Robledo, β decay of even-A nuclei within the interacting boson model with input based on nuclear density functional theory, Phys. Rev. C **101**, 044318 (2020).

[17] J. Engel, M. Bender, J. Dobaczewski, W. Nazarewicz, and R. Surman, β decay rates of *r*-process waiting-point nuclei in a self-consistent approach, Phys. Rev. C **60**, 014302 (1999).

[18] J. J. Cuenca-Garcıa, G. Martínez-Pinedo, K. Langanke *et al.*, Shell model half-lives for *r*-process $N = 82$ nuclei, Eur. Phys. J. A **34**, 99 (2007).

[19] G. Martínez-Pinedo and K. Langanke, Shell-Model Half-Lives for $N = 82$ Nuclei and their Implications for the *r* Process, Phys. Rev. Lett. **83**, 4502 (1999).

[20] K. Langanke and G. Martínez-Pinedo, Nuclear weak-interaction processes in stars, Rev. Mod. Phys. **75**, 819 (2003).

[21] J. Suhonen, Effective value of $g_{\rm A}$ in β and $\beta\beta$ decays, J. Phys.: Conf. Ser. **1056**, 012056 (2018).

[22] A. Kumar, P. C. Srivastava, and T. Suzuki, Shell model results for nuclear β^--decay properties of *sd*-shell nuclei, Prog. Theor. Exp. Phys. **2020**, 033D01 (2020).

[23] E. K. Warburton, Core polarization effects on spin-dipole and first-forbidden β-decay operators in the lead region, Phys. Rev. C **42**, 2479 (1990).

[24] E. K. Warburton, First-forbidden decay in the lead region and mesonic enhancement weak axial current, Phys. Rev. C **44**, 233 (1991).

[25] E. K. Warburton, Mesonic Enhancement of the Weak Axial-Vector Current Evaluated from β Decay in the Lead Region, Phys. Rev. Lett. **66**, 1823 (1991).

[26] L. Rydström *et al.*, Structure of proton-deficient nuclei near ^{208}Pb, Nucl. Phys. A **512**, 217 (1990).

[27] Q. Zhi, E. Caurier, J. J. Cuenca-Garcia, K. Langanke, G. Martinez-Pinedo, and K. Sieja, Shell-model half-lives including first-forbidden contributions for *r*-process waiting-point nuclei, Phys. Rev. C **87**, 025803 (2013).

[28] E. K. Warburton and B. A. Brown, Appraisal of the Kuo-Herling shell-model interaction and application to $A =$ 210–212 nuclei, Phys. Rev. C **43**, 602 (1991).

[29] B. Andel *et al.*, New β-decaying state in ^{214}Bi, Phys. Rev. C **104**, 054301 (2021).

[30] J. Suhonen, *From Nucleons to Nucleus: Concept of Microscopic Nuclear Theory* (Springer, Berlin 2007).

[31] H. Behrens and W. Bühring, *Electron Radial Wave Functions and Nuclear Beta-Decay* (Clarendon, Oxford, 1982).

[32] H. F. Schopper, *Weak interaction and Nuclear Beta Deacy* (North-Holland, Amsterdam, 1996).

[33] B. A. Brown and B. H. Wildenthal, Experimental and theoretical Gamow-Teller beta-decay observables for the *sd*-shell nuclei, At. Data Nucl. Data Tables **33**, 347 (1985).

[34] M. Haaranen, J. Kotila, and J. Suhonen, Spectrum-shape method and the next-to-leading-order terms of the β-decay shape factor, Phys. Rev. C **95**, 024327 (2017).

[35] H. Behrens and W. Bühring, Nuclear beta-decay, Nucl. Phys. A **162**, 111 (1971).

[36] M. T. Mustonen, M. Aunola, and J. Suhonen, Theoretical description of the fourth-forbidden nonunique β decays of ^{113}Cd and ^{115}In, Phys. Rev. C **73**, 054301 (2006).

[37] A. Kumar, P. C. Srivastava, J. Kostensalo, and J. Suhonen, Second-forbidden nonunique β^- decays of ^{24}Na and ^{36}Cl assessed by the nuclear shell model, Phys. Rev. C **101**, 064304 (2020).

[38] A. Kumar, P. C. Srivastava, and J. Suhonen, Second-forbidden nonunique β^- decays of ^{59,60}Fe: possible candidates for $g_{\rm A}$ sensitive electron spectral-shape measurements, Eur. Phys. J. A **57**, 225 (2021).

[39] B. A. Brown and W. D. M. Rae, The shell-model code NuShellX@MSU, Nucl. Data Sheets **120**, 115 (2014).

[40] N. Shimizu, T. Mizusaki, Y. Utsuno, and Y. Tsunoda, Thick-restart block Lanczos method for large-scale shell-model calculations, Comput. Phys. Commun. **244**, 372 (2019).

[41] C. Patrignami (Particle Data Group), Review of particle physics, Chin. Phys. C **40**, 100001 (2016).

[42] V. Kumar, P. C. Srivastava, and H. Li, Nuclear β^- decay half-lives for fp and fpg shell nuclei, J. Phys. G: Nucl. Part. Phys. **43**, 105104 (2016).

[43] J. Duflo and A. P. Zuker, Microscopic mass formulas, Phys. Rev. C **52**, R23(R) (1995).

[44] E. Caurier, G. Martinez-Pinedo, F. Nowacki, A. Poves, J. Retamosa, and A. P. Zuker, Full $0\hbar\omega$ shell-model calculation of the binding energies of the $1f_{7/2}$ nuclei, Phys. Rev. C **59**, 2033 (1999).

[45] P. Choudhary, A. Kumar, P. C. Srivastava, and T. Suzuki, Structure of ^{46,47}Ca from the β^- decay of ^{46,47}K in the framework of the nuclear shell-model, Phys. Rev. C **103**, 064325 (2021).

[46] I. S. Towner, Enhancement in axial-charge matrix elements from meson-exchange currents, Nucl. Phys. A **542**, 631 (1992).

[47] M. Haaranen, P. C. Srivastava, and J. Suhonen, Forbidden nonunique β decays and effective values of weak coupling constants, Phys. Rev. C **93**, 034308 (2016).

[48] Data extracted using the NNDC World Wide Web site from the ENSDF, https://www.nndc.bnl.gov/ensdf/

[49] S. Yoshida, Y. Utsuno, N. Shimizu, and T. Otsuka, Systematic shell-model study of β-decay properties and Gamow-Teller strength distributions in $A \approx 40$ neutron-rich nuclei, Phys. Rev. C **97**, 054321 (2018).

[50] P. Möller, B. Pfeiffer, and K. L. Kratz, New calculations of gross β-decay properties for astrophysical applications: Speeding up the classical *r* process, Phys. Rev. C **67**, 055802 (2003).

[51] T. Marketin, L. Huther, and G. Martínez-Pinedo, Large-scale evaluation of β-decay rates of *r*-process nuclei with the inclusion of first-forbidden transitions, Phys. Rev. C **93**, 025805 (2016).

[52] J. Suhonen and J. Kostensalo, Double β decay and the axial strength, Front. Phys. **7**, 29 (2019).

[53] H. A. Weidenmüller, First-forbidden beta decay, Rev. Mod. Phys. **33**, 574 (1961).